Multiple-relaxation-time color-gradient lattice Boltzmann model for simulating two-phase flows with high density ratio

Yan Ba,[1,2] Haihu Liu,[1] Qing Li,[3] Qinjun Kang,[2] and Jinju Sun[1,4,*]

[1]*School of Energy and Power Engineering, Xi'an Jiaotong University, 28 West Xianning Road, Xi'an 710049, China*

[2]*Los Alamos National Laboratory, Los Alamos, New Mexico 87545, USA*

[3]*School of Energy Science and Engineering, Central South University, Changsha 410083, China*

[4]*Collaborative Innovation Center for Advance Aero-Engine (CICAAE), Beijing, China*

(Received 18 December 2015; revised manuscript received 4 July 2016; published 15 August 2016)

In this paper we propose a color-gradient lattice Boltzmann (LB) model for simulating two-phase flows with high density ratio and high Reynolds number. The model applies a multirelaxation-time (MRT) collision operator to enhance the stability of the simulation. A source term, which is derived by the Chapman-Enskog analysis, is added into the MRT LB equation so that the Navier-Stokes equations can be exactly recovered. Also, a form of the equilibrium density distribution function is used to simplify the source term. To validate the proposed model, steady flows of a static droplet and the layered channel flow are first simulated with density ratios up to 1000. Small values of spurious velocities and interfacial tension errors are found in the static droplet test, and improved profiles of velocity are obtained by the present model in simulating channel flows. Then, two cases of unsteady flows, Rayleigh-Taylor instability and droplet splashing on a thin film, are simulated. In the former case, the density ratio of 3 and Reynolds numbers of 256 and 2048 are considered. The interface shapes and spike and bubble positions are in good agreement with the results of previous studies. In the latter case, the droplet spreading radius is found to obey the power law proposed in previous studies for the density ratio of 100 and Reynolds number up to 500.

DOI: 10.1103/PhysRevE.94.023310

I. INTRODUCTION

In recent years, the lattice Boltzmann (LB) method has developed to be a powerful tool for simulating multiphase and multicomponent flows [1–3]. The LB method is a mesoscopic computational method which solves the kinetic-based evolution equations for the distribution functions instead of the macroscopic governing equations in conventional computational fluid dynamics (CFD) methods. Due to its kinetic nature, the LB method is advantageous over conventional CFD methods in modeling multiphase flows. For example, in conventional CFD methods such as the volume of fluid [4,5] and level-set methods [6,7], the interfacial behavior is often obtained by solving a transport equation of the volume fraction (level-set function) and implementing an interface reconstruction (re-initialization) process, which are complicated and difficult to realize. However, in the LB method, the multiphase interface can be automatically captured and the interfacial dynamics can be easily modeled by the incorporation of intermolecular-level interactions.

Generally, the existing multiphase LB models can be classified into four categories: color-gradient model [8], pseudopotential model [3,9–11], free-energy model [12], and mean-field model [13,14]. In the present study we focus on the color-gradient model. The color-gradient model possesses many strengths in simulating multiphase and multicomponent flows, including strict mass conservation for each fluid, the flexibility in adjusting the interfacial tension, and the stability for a broad range of viscosity ratios. In addition, it can be implemented with much ease, and the numerical results in the literature [15,16] show that the color-gradient model is of high accuracy and relatively low spurious velocities at various viscosity ratios. A color-gradient model was proposed by Gunstensen *et al.* [8] in 1991, which is based on the cellular automata model for immiscible two-phase flows developed by Rothmann and Keller [17]. This model introduces two distribution functions to represent two immiscible fluids (i.e., red and blue fluids), and uses a color-gradient-related perturbation operator to generate the interfacial tension, and a recoloring step to separate the two fluids. By introducing the freedom in the rest equilibrium distribution functions, Grunau *et al.* [18] modified the Gunstensen's model to allow for a small variation of density. Later, using the similar idea of Grunau *et al.*, Reis and Phillips [15] developed a two-dimensional nine-velocity (D2Q9) version of the color-gradient model, which could simulate the density ratio up to 18.5 in the droplet coalescence test. Latva-Kokko and Rothman [19] replaced Gunstensen's maximization recoloring step with a formulaic segregation algorithm, which removes the lattice pinning problem and at the same time reduces spurious velocities, but widens the interface on a certain level. Lishchuk *et al.* [20] introduced the perturbation step with a direct forcing term, which effectively reduces spurious velocities arising in the vicinity of the interface. Liu *et al.* [16] proposed a three-dimensional color-gradient model and derived a generalized perturbation operator that can recover the correct form of the interfacial tension in the Navier-Stokes equations (NSEs).

With the above advances, the color-gradient LB models have been improved significantly and widely used to study multiphase and multicomponent flows [21–23]. Recently, however, some critical issues about the ability of the color-gradient models in dealing with high density ratio flows have been raised by Leclaire *et al.* [24] and Huang *et al.* [25]. By replacing the recoloring step with a formulaic segregation algorithm, Leclaire *et al.* [24] improved the model of Reis

*Corresponding author: jjsun@mail.xjtu.edu.cn

and Phillips [15] for binary fluids with variable density and viscosity ratios. However, when simulating the layered channel flow with the density ratios larger than unity, they found a large discrepancy between the numerical and analytical solutions. This discrepancy was later identified by Huang *et al.* [25] to arise from an unwanted additional term in the momentum equations, which is not negligibly small for nonunity density ratios. In order to eliminate the unwanted term, Huang *et al.* [25] further proposed to add a source term into the evolution equation of distribution functions. Their model showed an apparently enhanced performance in simulating the layered channel flow for the density ratios up to 8, but the evaluation of the source term may lead to considerable numerical errors at higher density ratios. Recently, Leclaire *et al.* [26] used an enhanced equilibrium distribution function to simulate the layered Couette flows, and found good agreement between the numerical and analytical solutions for the density ratios up to 1000. Lishchuk *et al.* [27] modeled the high density ratio two-phase flows by introducing the shear-dependent forces, which act in the region of the interface and could compensate the relative fluid motion caused by inertia. They successfully simulated the static bubble case and the bubble rising case for the density ratios respectively up to 1000 and 10. On the other hand, the multiple-relaxation-time (MRT) collision operator [28] has been recently adopted in the color-gradient LB models to enhance the numerical stability [21,29,30]. In particular, in the latest work of Leclaire *et al.* [31], the MRT collision operator was combined with the enhanced equilibrium distribution functions [26], which enables their model to be capable of simulating high density ratio flows for both steady and unsteady cases.

Although the aforementioned studies have improved the performance of the color-gradient LB models for high density ratio flows, significant efforts are still needed because most of them only focused on the simulation of steady flows. The model's capability for unsteady two-phase flows with complex interfacial behaviors and/or high Reynolds numbers have not been considered convincingly even at the density ratios of $O(10)$. In contrast, the free-energy and the pseudopotential models have gained great confidence in the simulation of high density ratio two-phase flows. For example, Inamuro *et al.* [32] successfully simulated the rise of bubbles in a liquid with the density ratios up to 1000 by using a variant of the free-energy model, in which a pressure correction is applied to enforce the continuity condition after every collision-propagation step. Similar density contrasts for the droplet splashing were achieved by Lee and Lin [33], who established a model based on the phase field free-energy theory through a stable discretization of the LB equations.

In this paper we propose a color-gradient LB model for simulating immiscible two-phase flows, which is capable of handling flows with high density ratio and high Reynolds number. The proposed model has several distinct features compared with previous studies [25–27,30,31] in the following aspects: (1) the use of a modified equilibrium density distribution function that is derived from the third-order Hermite expansion [30,34]; (2) the enhancement of the numerical stability by means of MRT collision operator corresponding to the modified equilibrium density distribution function; and (3) the incorporation of a simple source term into an MRT LB equation so as to recover the target NSEs. To validate the proposed model, we first simulate a static droplet and the layered channel flow for the density ratios up to 1000 and compare the simulation results with the analytical solutions. Then, two unsteady flow cases that involve complex interfacial dynamics are simulated, i.e., the Rayleigh-Taylor instability with the density ratio of 3 and the Reynolds numbers up to 2048, and a droplet splashing on a thin film with the density ratio of 100 and the Reynolds numbers up to 500. To the best of our knowledge, the unsteady flows with the density ratios and Reynolds numbers considered in this work have not been simulated satisfactorily by the previous color-gradient models.

II. NUMERICAL MODEL

In the present model, two immiscible fluids are represented as a red fluid and a blue fluid, respectively. The distribution function f_i^k is introduced to represent the fluid k, where $k = R$ or B denotes the color ("red" or "blue"), and i is the lattice velocity direction. The total distribution function is defined as $f_i = f_i^R + f_i^B$. The evolution of the distribution function is expressed by the following LB equation:

$$f_i^k(\mathbf{x} + \mathbf{e}_i\delta_t, t + \delta_t) = f_i^k(\mathbf{x}, t) + \mathbf{\Omega}_i^k\left(f_i^k(\mathbf{x}, t)\right), \tag{1}$$

where $\mathbf{x}$ and t are the position and time, $\mathbf{e}_i$ is the lattice velocity in the ith direction, δ_t is the time step, and $\mathbf{\Omega}_i^k$ is the collision operator.

The collision operator Ω_i^k consists of three parts:

$$\mathbf{\Omega}_i^k = \left(\mathbf{\Omega}_i^k\right)^{(3)}\left[\left(\mathbf{\Omega}_i^k\right)^{(1)} + \left(\mathbf{\Omega}_i^k\right)^{(2)}\right], \tag{2}$$

where $(\mathbf{\Omega}_i^k)^{(1)}$ is the single phase collision operator, $(\mathbf{\Omega}_i^k)^{(2)}$ is the perturbation operator which generates an interfacial tension, and $(\mathbf{\Omega}_i^k)^{(3)}$ is the recoloring operator which is used to produce the phase segregation and maintain the phase interface.

A. Single phase collision operator

In a color-gradient LB model, the single phase collision operator often used is the Bhatnagar-Gross-Krook (BGK) collision operator with the rest particle equilibrium distributions relying upon the density ratio [15,16,24,29,35]. In this subsection we will first show that the use of BGK collision operator fails to recover the correct NSEs in dynamic problems when the fluids have unequal densities, and then propose a MRT scheme together with a simple correction term so that the target NSEs can be recovered exactly.

1. BGK collision operator and unwanted term in NSEs

Using the BGK approximation, the single phase collision operator $(\mathbf{\Omega}_i^k)^{(1)}$ in color-gradient models can be written as

$$\left(\mathbf{\Omega}_i^k\right)^{(1)} = -\boldsymbol{\omega}^k\left[f_i^k - f_i^{k,(\mathrm{eq})}\right], \tag{3}$$

in which $\boldsymbol{\omega}^k$ is the relaxation parameter [35] and $f_i^{k,(\mathrm{eq})}$ is the equilibrium distribution function [15]:

$$f_i^{k,(\mathrm{eq})}(\rho^k, \mathbf{u}) = \rho^k\left(\phi_i^k + W_i\left[\frac{3\mathbf{e}_i\cdot\mathbf{u}}{c^2} + \frac{9(\mathbf{e}_i\cdot\mathbf{u})^2}{2c^4} - \frac{3(\mathbf{u})^2}{2c^2}\right]\right), \tag{4}$$

where c is the lattice speed, W_i is the weight parameter defined in the D2Q9 lattice model [10], ϕ_i^k is a parameter which is related to the density ratio of the two fluids, ρ^k is the density of each fluid, and $\mathbf{u}$ is the velocity of the fluid mixture. The macroscopic variables are obtained by the mass and momentum conservations:

$$\begin{aligned}\rho^k &= \sum_i f_i^k = \sum_i f_i^{k,(\mathrm{eq})},\\ \rho\mathbf{u} &= \sum_i \sum_k \mathbf{e}_i f_i^k = \sum_i \sum_k \mathbf{e}_i f_i^{k,(\mathrm{eq})},\end{aligned} \tag{5}$$

in which $\rho = \sum_k \rho^k$ is the density of the fluid mixture. Note that the parameter ϕ_i^k in Eq. (4) is equal to W_i in the most LB models, while in some Shan-Chen models (e.g., the model of Kang *et al.* [11]) and in color-gradient models [15,24], it is expressed as a general form:

$$\phi_i^k = \begin{cases}\alpha^k, & i = 0,\\ (1-\alpha^k)/5, & i = 1,2,3,4,\\ (1-\alpha^k)/20, & i = 5,6,7,8,\end{cases} \tag{6}$$

in which α^k is a free parameter related to the speed of sound of each fluid by $(c_s^k)^2 = \frac{3}{5}(1-\alpha^k)$, c_s^k controls the hydrodynamic pressure of each phase p^k through the equation of state $p^k = \rho^k (c_s^k)^2$, and the hydrodynamic pressure of the fluid mixture is calculated by $p = \sum_k p^k$. The stable interface assumption requires the free parameters α^R and α^B to satisfy the following relation [15]:

$$\gamma = \frac{\rho^{R0}}{\rho^{B0}} = \frac{1-\alpha^B}{1-\alpha^R}, \tag{7}$$

where ρ^{R0} and ρ^{B0} are the densities of the pure red and blue fluids, and γ represents the density ratio. The constraint of $0 \leqslant \alpha^k \leqslant 1$ should be satisfied to avoid the unreal value of speed of sound and negative value of fluid density.

Taking the zeroth- to third-order velocity moments of the equilibrium distribution functions, we have

$$\begin{aligned}\sum_i f_i^{k,(\mathrm{eq})} &= \rho^k,\\ \sum_i f_i^{k,(\mathrm{eq})} e_{i\alpha} &= \rho^k u_\alpha,\\ \sum_i f_i^{k,(\mathrm{eq})} e_{i\alpha} e_{i\beta} &= \rho^k u_\alpha u_\beta + \rho^k \left(c_s^k\right)^2 \delta_{\alpha\beta},\\ \sum_i f_i^{k,(\mathrm{eq})} e_{i\alpha} e_{i\beta} e_{i\gamma} &= \frac{1}{3}\rho^k c^2 (u_\gamma \delta_{\alpha\beta} + u_\beta \delta_{\alpha\gamma} + u_\gamma \delta_{\alpha\beta}).\end{aligned} \tag{8}$$

Note in the above equation that $(c_s^k)^2$ in the second-order moment is usually not equal to $\frac{1}{3}c^2$ in the third-order moment for binary fluids with unequal densities, which can lead to an unwanted error term (argued recently by Huang *et al.* [25]) in the recovered momentum equations [16]:

$$\begin{aligned}U_\alpha^k = \left(\frac{1}{\boldsymbol{\omega}^k} - \frac{1}{2}\right)\left[\frac{1}{3}c^2 - \left(c_s^k\right)^2\right]\partial_\beta[u_\beta \partial_\alpha(\rho^k) + u_\alpha \partial_\beta(\rho^k)\\ + \partial_\gamma(\rho^k u_\gamma)\delta_{\alpha\beta}].\end{aligned} \tag{9}$$

To reduce or eliminate the error term, a direct way is to add a source term C_i^k into the single phase collision operator, as previously done by Huang *et al.* [25]:

$$C_i^k = -W_i U_\alpha^k e_{i\alpha} \frac{3}{c^2}. \tag{10}$$

This source term is able to enhance the numerical accuracy in simulating the layered channel flow for the density ratio up to 8, but such a simple treatment cannot lead to the correct NSEs and the evaluation of the density gradients may introduce considerable numerical errors for higher density ratio flows. Leclaire *et al.* [26] later used an enhanced equilibrium distribution function, by which one can recover the correct NSEs with the error terms that can be neglected under some conditions. Their model can provide accurate simulation results for two-layered Couette flows with density ratios up to 1000.

2. *MRT collision operator*

In this subsection we will provide a collision operator to deal with two-phase flows with high density ratios, which can exactly recover the target NSEs by adding a simple correction term.

In the LB method, the MRT model is demonstrated to have better numerical stability than its BGK counterpart [28], and thus it is adopted in this study. Using the MRT collision model, the single phase collision operator can be written as

$$\left(\boldsymbol{\Omega}_i^k\right)^{(1)} = \sum_j (\mathbf{M}^{-1}\mathbf{S})_{ij}\left(m_j^k - m_j^{k,(\mathrm{eq})}\right) + \sum_j (\mathbf{M}^{-1})_{ij} C_j^k, \tag{11}$$

where C_j^k is a source term and will be defined later, and $\mathbf{S}$ is the diagonal matrix given by

$$\begin{aligned}\mathbf{S} &= \mathrm{diag}(s_0, s_1, s_2, s_3, s_4, s_5, s_6, s_7, s_8)\\ &= \mathrm{diag}(0, s_e, s_\varsigma, 0, s_q, 0, s_q, s_v, s_v),\end{aligned} \tag{12}$$

where the element s_i represents the relaxation parameter. Considering the suggestions in Ref. [28], the relaxation parameters are chosen as $s_e = 1.25$, $s_\varsigma = 1.14$, $s_q = 1.6$, and s_v is related to the dynamic viscosity of the two fluids. $\mathbf{M}$ is a linear orthogonal transformation matrix that projects f_i^k in the discrete velocity space to m_i^k in the moment space, and $\mathbf{M}$ and its inverse matrix $\mathbf{M}^{-1}$ are given in Appendix A. The distribution function in moment space is obtained by $m_i^k = \sum_j \mathbf{M}_{ij} f_j^k$ and can be written as

$$\begin{aligned}\mathbf{m}^k &= \left(m_0^k, m_1^k, m_2^k, m_3^k, m_4^k, m_5^k, m_6^k, m_7^k, m_8^k\right)^T\\ &= \left(\rho^k, e^k, \varsigma^k, j_x^k, q_x^k, j_y^k, q_y^k, p_{xx}^k, p_{xy}^k\right)^T,\end{aligned} \tag{13}$$

where e^k is the energy mode, ς^k is related to energy square, (j_x^k, j_y^k) are the momentum components, (q_x^k, q_y^k) are the energy flux, and (p_{xx}^k, p_{xy}^k) are related to the diagonal and off-diagonal components of the stress tensors [28]. In the same way, the equilibrium distribution functions in moment space $m_i^{k,(\mathrm{eq})}$ in Eq. (11) is obtained by $m_i^{k,(\mathrm{eq})} = \sum_j \mathbf{M}_{ij} f_j^{k,(\mathrm{eq})}$. In our model, an equilibrium distribution function different from Eq. (4) is

applied

$$f_i^{k,(\mathrm{eq})}(\rho,\mathbf{u}) = \rho^k\phi_i^k + \rho^k W_i\left\{\frac{3\mathbf{e}_i\cdot\mathbf{u}}{c^2}\left[1+\frac{1}{2}\left(\frac{3\left(c_s^k\right)^2}{c^2}-1\right)\left(\frac{3(\mathbf{e}_i)^2}{c^2}-4\right)\right]+\frac{9(\mathbf{e}_i\cdot\mathbf{u})^2}{2c^4}-\frac{3(\mathbf{u})^2}{2c^2}\right\}, \tag{14}$$

which is derived based on the third-order Hermite expansion of the Maxwellian distribution [30,34]. It is easily demonstrated that the zeroth- to second-order velocity moments of the equilibrium distribution function Eq. (14) are the same as those shown in Eq. (8). Taking the third-order velocity moment of $f_i^{k,(\mathrm{eq})}$, however, one obtains [34]

$$\sum_i f_i^{k,(\mathrm{eq})} e_{i\alpha}e_{i\beta}e_{i\gamma} = \begin{cases}\frac{1}{3}\rho_k c^2(u_\gamma\delta_{\alpha\beta}+u_\beta\delta_{\alpha\gamma}+u_\gamma\delta_{\alpha\beta}), & \text{if } i=j=k,\\ \rho_k\left(c_s^k\right)^2(u_\gamma\delta_{\alpha\beta}+u_\beta\delta_{\alpha\gamma}+u_\gamma\delta_{\alpha\beta}), & \text{otherwise.}\end{cases} \tag{15}$$

It can be seen that the off-diagonal elements of the third-order velocity moment can completely cancel the error term U_α^k in Eq. (9) [34], but the diagonal elements cannot.

Using the equilibrium distribution function $f_i^{k,(\mathrm{eq})}$ in Eq. (14), $m_i^{k,(\mathrm{eq})}$ can be obtained as follows:

$$\begin{aligned}\mathbf{m}^{k,(\mathrm{eq})} &= \left(m_0^{k,(\mathrm{eq})},m_1^{k,(\mathrm{eq})},\ldots,m_8^{k,(\mathrm{eq})}\right)^T = \left(\rho^k,e^{k,(\mathrm{eq})},\varsigma^{k,(\mathrm{eq})},j_x^k,q_x^{k(\mathrm{eq})},j_y^k,q_y^{k,(\mathrm{eq})},p_y^{k,(\mathrm{eq})},p_y^{k,(\mathrm{eq})}\right)^T\\ &= \rho^k\left(1,-3.6\alpha^k-0.4+3\mathbf{u}^2,5.4\alpha^k-1.4-3\mathbf{u}^2,u_x,(-1.8\alpha^k-0.2)u_x,u_y,(-1.8\alpha^k-0.2)u_y,u_x^2-u_y^2,u_xu_y\right)^T.\end{aligned} \tag{16}$$

Through the Chapman-Enskog multiscale analysis (see Appendix B), the exact NSEs can be recovered if the source term of each phase $\mathbf{C}^k$ in Eq. (11) is chosen as

$$\mathbf{C}^k = \left[0,C_1^k,0,0,0,0,0,C_7^k,0\right]^T, \tag{17}$$

where

$$\begin{aligned}C_1^k &= 3(1-s_e/2)(\partial_x Q_x+\partial_y Q_y),\\ C_7^k &= (1-s_v/2)(\partial_x Q_x-\partial_y Q_y),\\ Q_x &= (1.8\alpha^k-0.8)\rho^k u_x,\\ Q_y &= (1.8\alpha^k-0.8)\rho^k u_y.\end{aligned} \tag{18}$$

Compared with Eq. (10), this source term only contains the first-order derivatives, and only two of the moment functions need to be corrected. As shown in Appendix B, the dynamic viscosity μ of the fluid mixture is related to s_v by

$$\mu = \delta_t\left(\frac{1}{s_v}-\frac{1}{2}\right)p. \tag{19}$$

In our numerical simulations, the derivatives of a variable ψ, e.g., Q_x and Q_y in Eq. (17), can be calculated by the nine-point isotropic finite difference approximation, i.e.,

$$\partial_\alpha\psi(\mathbf{x}) = \frac{3}{c^2}\sum_i W_i\psi(\mathbf{x}+\mathbf{e}_i\delta_t)e_{i\alpha}. \tag{20}$$

The phase field function ρ^N is an important parameter in the color-gradient models, and its gradient $\nabla\rho^N$ is used to identify the interface and calculate the interfacial force. Usually, ρ^N is defined by $\rho^N=(\rho^R-\rho^B)/(\rho^R+\rho^B)$ [8,15]. This definition, however, becomes increasingly incorrect in identifying the interface as the density ratio increases. Thus, Leclaire *et al.* [36] proposed a formulation to calculate the gradient of the phase field, i.e.,

$$\nabla\rho^N = \frac{\rho^B}{\rho}\nabla\left(\frac{\rho^R}{\rho}\right)-\frac{\rho^R}{\rho}\nabla\left(\frac{\rho^B}{\rho}\right).$$

In the present model we use the following definition:

$$\rho^N = \left(\frac{\rho^R}{\rho^{R0}}-\frac{\rho^B}{\rho^{B0}}\right)\Big/\left(\frac{\rho^R}{\rho^{R0}}+\frac{\rho^B}{\rho^{B0}}\right). \tag{21}$$

In this way, the interface position can be well represented by the $\rho^N=0$ contour; and also, Eq. (21) will reduce to the conventional definition when both fluids have equal densities.

To account for unequal viscosity of the two fluids and ensure the smoothness of the relaxation parameter s_v across the interface, s_v is calculated as

$$s_v = \begin{cases}s_v^R, & \rho^N > \delta,\\ g^R(\rho^N), & \delta\geqslant\rho^N>0,\\ g^B(\rho^N), & 0\geqslant\rho^N>-\delta,\\ s_v^B, & \rho^N<-\delta,\end{cases} \tag{22}$$

where s_v^k is the relaxation parameter of the fluid k, which is given by $s_v^k = 1/(\mu^k/p^k+0.5)$; δ is a free parameter associated with the interface thickness and is taken as 0.1 in the present study; and g^R and g^B are parabolic functions of the phase field function ρ^N, and they are given by Reis *et al.* [15].

B. Perturbation operator

The perturbation operator $(\mathbf{\Omega}_i^k)^{(2)}$ is responsible for generating the interfacial tension, and can be expressed as [37]

$$\left(\mathbf{\Omega}_i^k\right)^{(2)} = A^k W_i\left(1-\frac{\omega^k}{2}\right)[3(\mathbf{e}_i-\mathbf{u})+9(\mathbf{e}_i\cdot\mathbf{u})\mathbf{e}_i]\cdot\mathbf{F}_s, \tag{23}$$

where A^k is the fraction of interfacial tension contributed by the fluid k, and satisfies $\sum_k A^k=1$, and $\mathbf{F}_s$ is the interfacial tension. Here we follow the previous researches [20,38] and model the interfacial using the continuum surface force (CSF) model, which can effectively reduce spurious currents and improve the isotropy of the interface. Using the definition of ρ^N in Eq. (21), the interfacial tension can be expressed as

$$\mathbf{F}_s = -\tfrac{1}{2}\sigma K\nabla\rho^N, \tag{24}$$

where σ is the interfacial tension coefficient, and K is the local curvature of the interface given by

$$K = -\nabla_S \cdot \mathbf{n}, \tag{25}$$

in which $\nabla_S = (\mathbf{I} - \mathbf{nn}) \cdot \nabla$ is the surface gradient operator and $\mathbf{n} = -\nabla\rho^N/|\nabla\rho^N|$ is the outward-pointing unit normal vector of the interface. In 2D, the curvature of the interface can be written as

$$K = n_x n_y \left(\frac{\partial}{\partial y} n_x + \frac{\partial}{\partial x} n_y\right) - n_x^2 \frac{\partial}{\partial y} n_y - n_y^2 \frac{\partial}{\partial x} n_x. \tag{26}$$

In this work, to be consistent with the single phase collision operator, the perturbation step is also implemented in the MRT framework. In moment space, the perturbation operator is written as

$$F_i^k(\mathbf{x},t) = \sum_j \mathbf{M}_{ij} \left(\mathbf{\Omega}_j^k\right)^{(2)}, \tag{27}$$

where

$$\begin{aligned}\mathbf{F}^k(\mathbf{x},t) &= \left(F_0^k,\ F_1^k,\ \ldots,\ F_8^k\right)^T \\ &= A^k\left(1 - \frac{\boldsymbol{\omega}^k}{2}\right)[0, 6(u_x F_{sx} + u_y F_{sy}), \\ &\quad -6(u_x F_{sx} + u_y F_{sy}), F_{sx}, -F_{sx}, F_{sy}, -F_{sy}, \\ &\quad \times 2(u_x F_{sx} - u_y F_{sy}), (u_x F_{sy} + u_y F_{sx})]^T. \end{aligned} \tag{28}$$

From Eq. (24) it can be clearly seen that the interfacial tension is applied only at the lattice sites where two fluids coexist. In the presence of the interfacial tension, the velocity should be redefined to correctly recover the NSEs [35], i.e.,

$$\rho^k \mathbf{u} = \sum_i \sum_k \mathbf{e}_i f_i^k + \frac{1}{2}\mathbf{F}_s. \tag{29}$$

C. Recoloring operator

To promote phase segregation and maintain a reasonable interface, the segregation operator proposed by Latva-Kokko and Rothman [19] is used, and it is given by

$$\begin{aligned}\left(\mathbf{\Omega}_i^R\right)^{(3)}(f_i') \equiv f_i^{R''} &= \frac{\rho^R}{\rho} f_i' + \beta W_i \frac{\rho^R \rho^B}{\rho} \cos(\varphi_i)|\mathbf{e}_i|, \\ \left(\mathbf{\Omega}_i^B\right)^{(3)}(f_i') \equiv f_i^{B''} &= \frac{\rho^B}{\rho} f_i' + \beta W_i \frac{\rho^R \rho^B}{\rho} \cos(\varphi_i)|\mathbf{e}_i|, \end{aligned} \tag{30}$$

where f_i' is the post-perturbation value of the total distribution function; $f_i^{R''}$ and $f_i^{B''}$ are post-segregation (recolored) distribution functions of the red and blue fluids, respectively; φ_i is the angle between the color gradient $\nabla\rho^N$ and the lattice direction $\mathbf{e}_i$; and β is a parameter associated with the interface thickness and should take a value between zero and unity.

Halliday *et al.* [38] and Hollis *et al.* [39] have identified that a combination of the segregation operator Eq. (30) and Guo *et al.*'s forcing method of Eq. (23) for the interfacial tension cannot lead to the phase field equation that satisfies the kinematic condition accurately. Specifically, the interface is accelerated relative to the local fluid due to the presence of unwanted terms in the recovered phase field equation. They also proposed a method to enforce the kinematic condition by applying a collision parameter perturbation that increases the local viscosity of the fluid mixture. However, the collision parameter perturbation was derived based on a static, spherical droplet suspended in an infinite domain, and its extension to complex interfacial dynamics remains unknown. Moreover, the collision parameter perturbation contains some numerical parameters to be determined, and it is still an open question on how to choose these numerical parameters. Thus, the segregation operator Eq. (30) with a combination with Guo *et al.*'s forcing method is still used in the present work for the sake of simplicity. Finally, it is worth noting that most of the existing color-gradient models used the present segregation operator without the enforcement of kinematic condition, but they have been extensively demonstrated to be accurate in predicting multicomponent flows such as bubble coalescence [24], droplet formation [23], and droplet deformation under a shear flow [16].

III. MODEL VERIFICATION

In this section we perform a series of numerical tests to assess the capability of the developed MRT color-gradient LB model, including the tests with theoretical solutions such as a static droplet and layered channel flow, as well as dynamic flows with complex interface evolution such as Rayleigh-Taylor instability and droplet splashing on a thin liquid layer. The layered channel flow and Rayleigh-Taylor instability are simulated using both the original color-gradient model proposed in our previous works [35] and our modified MRT model with a source term to show the differences between these two models. In order to keep consistency with our modified model, the original color-gradient model is also implemented in a MRT framework.

A. A static droplet test

First, a static droplet immersed in another fluid is simulated for different density ratios and interfacial tensions. Since the unwanted error term in Eq. (9) does not influence the results of static flows, we only use the modified MRT model in this test. According to the Laplace law, the droplet radius R and the pressure difference Δp inside and outside the droplet, in the steady state, satisfy the following equation:

$$\sigma = R\Delta p = R(p_{\text{in}} - p_{\text{out}}), \tag{31}$$

where p_{in} and p_{out} are the pressure inside and outside the droplet calculated by

$$\begin{aligned} p_{\text{in}} &= 0.6\rho_{\text{in}}^R(1-\alpha^R) + 0.6\rho_{\text{in}}^B(1-\alpha^B), \\ p_{\text{out}} &= 0.6\rho_{\text{out}}^R(1-\alpha^R) + 0.6\rho_{\text{out}}^B(1-\alpha^B), \end{aligned} \tag{32}$$

in which ρ_{in}^k and ρ_{out}^k denote the mean densities of the fluid k inside and outside the droplet.

A red circular droplet with the radius $R = 25$ is initially placed at the center of the computational domain with size 100×100 lattice cells. The density of the blue fluid is taken as $\rho^B = 1$, and the density of the red fluid is varied from 1 to 1000. The kinematic viscosities are set as $\nu^R = \nu^B = 0.1667$. Other parameters are chosen as $\alpha^B = 0.2$ and $\beta = 0.7$. This β corresponds to an interface thickness of 4–5 lattice

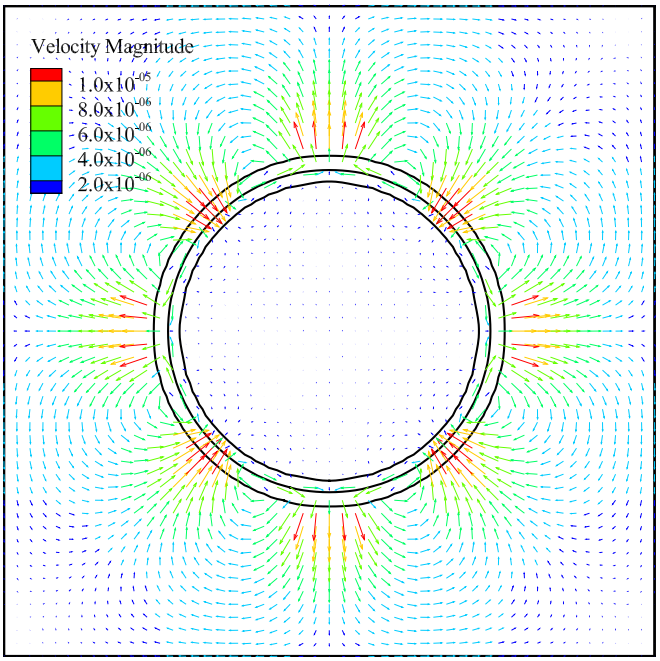

FIG. 1. Equilibrium droplet shape and velocity field for $\rho^R = 10$ and $\rho^B = 1$ at $\sigma = 0.1$.

grids. Periodic boundary conditions are imposed at all of the boundaries.

Figure 1 shows the equilibrium droplet shape and velocity field for $\rho^R = 10$ and $\rho^B = 1$ at $\sigma = 0.1$. Note that the interface is represented by three contours of ρ^N, i.e., $\rho^N = -0.9$, $\rho^N = 0$ and $\rho^N = 0.9$. In equilibrium state, spurious velocities are clearly visible in the entire computational domain, especially around the droplet interface. Table I shows the comparison between the calculated interfacial tension and the theoretical value, as well as the magnitude of the maximum spurious velocities for various density ratios and interfacial tensions. It is seen that the calculated interfacial tension σ_{cal} agrees well with the theoretical value σ_{th} for each of the simulations, and the relative error of interfacial tension, defined by $E = |\sigma_{\text{th}} - \sigma_{\text{cal}}|/\sigma_{\text{th}} \times 100\%$, changes insignificantly with the density ratio and increases slightly with the interfacial tension. It can also be observed that the maximum value of the spurious velocities $|\mathbf{u}|_{\max}$ increases with increasing density ratio or interfacial tension. For all the cases considered, $|\mathbf{u}|_{\max}$ keeps at a low level, much smaller than those obtained in previous studies [16,40].

TABLE I. A static droplet in a domain of 100×100 lattices for various density ratios and interfacial tensions.

ρ^R	α^B	σ_{th}	σ_{cal}	E	$\lvert\mathbf{u}\rvert_{\max} \times 10^5$
1	0.2	0.0120	0.0121	0.65%	0.716
1	0.2	0.0720	0.0726	0.84%	0.851
1	0.2	0.2400	0.2433	1.38%	2.09
2	0.2	0.1120	0.1090	0.95%	0.664
10	0.2	0.1320	0.1333	0.97%	1.29
30	0.2	0.1116	0.1125	0.83%	2.11
100	0.2	0.1000	0.1007	0.69%	6.81
1000	0.2	0.1000	0.1007	0.74%	12.5

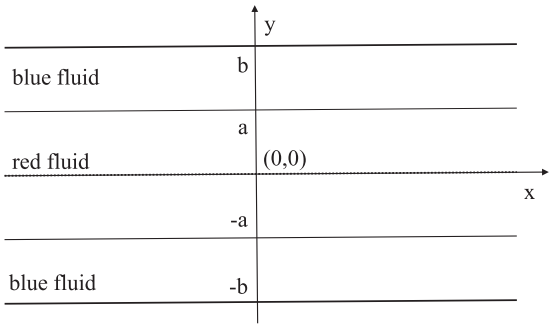

FIG. 2. Schematic of the layered two-phase flow in a 2D channel. The red (wetting) fluid flows in the region of $|y| < a$ and the blue (wetting) fluid flows in the region of $a < |y| < b$.

It should be noted that, to compare our model with other existing high density LB models, the static droplet test is also conducted using Lee's model of Ref. [41] for different density ratios. It is found that the spurious velocities produced by Lee's model are much smaller (at the level of 10^{-10}), while the relative errors of the surface tension remain at the same level for both models. Meanwhile, the computational time of Lee's model is nearly four times more than that of our model for the same simulation steps.

B. Layered two-phase flow in a 2D channel

Next, we simulate the layered two-phase immiscible channel flow between two parallel walls (illustrated in Fig. 2). Periodic boundary conditions are used at the left and right boundaries, and halfway bounce-back boundary conditions [42] are applied at the bottom and top walls. A constant body force $(G,0)$ is applied in the whole domain to maintain the flow in the channel.

The size of the computational domain is set as 10×100 lattices. The nonwetting fluid (red fluid) is located in the central region $|y| < a$ and the wetting fluid (blue fluid) in the region of $a \leqslant |y| \leqslant b$. Assuming the flow in the channel is Poiseuille type, the analytical solution for the velocity profile can be given as follows [21,43]:

$$u(y) = \begin{cases} A_1 y^2 + C_1 & (0 \leqslant |y| \leqslant a), \\ A_2 y^2 + B_2 y + C_2 & (a \leqslant |y| \leqslant b), \end{cases} \tag{33}$$

where the parameters are calculated by $A_1 = -\frac{G}{2\rho^R \nu^R}$, $A_2 = -\frac{G}{2\rho^B \nu^B}$, $B_2 = 2A_2 a + 2MA_1 a$, $C_1 = (A_2 - A_1)a^2 -$

TABLE II. Relative errors of the velocity obtained by the present model and the original color-gradient model at various density ratios.

					Relative error (E_u)	
Cases	α^B	ρ^R	ρ^B	M	Present model	Original color-gradient model
a	0.6	0.8	0.4	1	0.1646%	30.58%
b	0.2	0.4	0.8	1	0.1093%	49.25%
c	0.9	0.8	0.1	1	1.640%	195.3%
d	0.2	0.1	0.8	1	0.4633%	58.77%
e	0.9992	0.008	8	25	4.601%	
f	0.2	8	0.008	0.04	0.8673%	

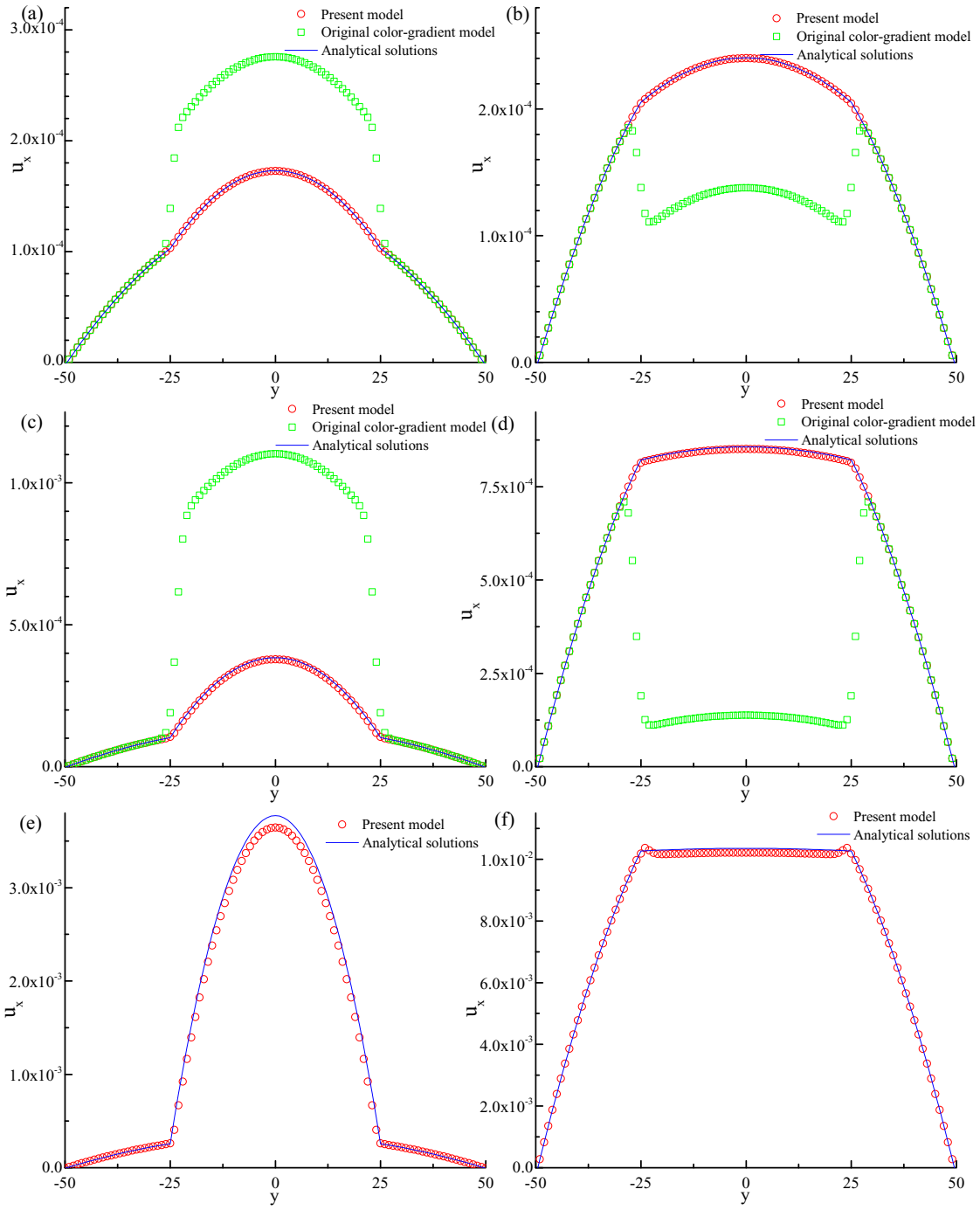

FIG. 3. Velocity profiles obtained by the present model and original color-gradient model for cases (a)–(f) in Table II. The analytical velocity profile is also plotted for comparison.

$B_2(b-a) - A_2b^2$, $C_2 = -A_2b^2 - B_2b$, and $M = \nu^R/\nu^B$ is the kinematic viscosity ratio of the two fluids. The relative error of the velocity between the simulation results and analytical solutions is defined as [25]

$$E_u = \frac{\sum_{y=-b}^{b} |u_x(x,y) - u_{x0}(x,y)|}{\sum_{y=-b}^{b} |u_{x0}(x,y)|} \times 100\%, \qquad (34)$$

in which the summation runs over all y at an arbitrary x, and u_{x0} is the analytical solution of the horizontal velocity.

Six different cases are simulated by both the present model and the original color-gradient model with the case-dependent simulation parameters described in Table II. Other simulation parameters are taken as $G = 1.5 \times 10^{-8}$ and $\beta = 0.7$. Figure 3 shows the comparison between simulated velocity profiles and the analytical solution for all of the cases considered. It can be clearly observed that the present model greatly improves the accuracy of the simulation results. Specifically, the velocity profile can be well predicted by the present model in all cases; but for the original color-gradient model, the predicted velocity profiles significantly deviate from the analytical ones

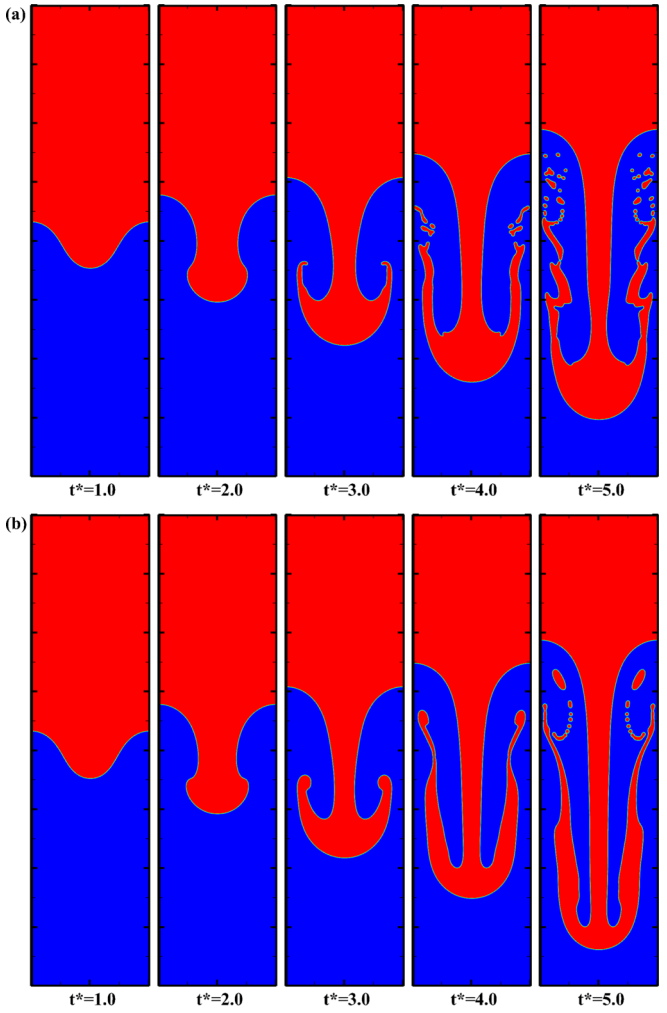

FIG. 4. Snapshots of the interface shape ($\rho^N = 0$) at different times for At = 0.5 and Re = 256, which are obtained by (a) the original color-gradient model and (b) the present model.

in the cases (a)–(d), which is attributed to the fact that the error term in Eq. (9) cannot be neglected due to the abrupt change of the momentum across the interface. In addition, the original color-gradient model is found to suffer from numerical instability at higher density ratios [see the cases (e) and (f)]. To quantify the simulated results, the relative error of the velocity E_u is presented in Table II. It can be seen that the relative error obtained by the original color-gradient model is too large to be acceptable, and it increases significantly with the density ratio. In contrast, the relative error obtained by the present model is generally very small except for case (e) ($\gamma = 0.001$), in which the relative error is as high as $E_u = 4.601\%$. We also note that the relative error can be reduced by grid refinement. For example, the relative error of the velocity will decrease to 2.317% for case (e) when the grid resolution is increased to 10×200 lattices. Based on the above results, we can conclude that the present model is more accurate than the original color-gradient model and can provide satisfactory prediction of the high-density-ratio two-phase flows.

C. Rayleigh-Taylor instability

When a heavy fluid is placed over a light one subjected to a slightly disturbed interface in a gravitational field, the interface will become unstable. This phenomenon is known as the Rayleigh-Taylor instability, which has been extensively studied both numerically and experimentally [33,44–47]. In our simulations, a fluid with density of ρ^R is placed above a fluid with density of ρ^B, and the Atwood number $\mathrm{At} = (\rho^R - \rho^B)/(\rho^R + \rho^B)$ is set to 0.5 in order to compare our results with the those reported in previous studies [44,48]. The size of the computational domain is $L \times 4L$, where $L = 256$ lattices in order to obtain grid-independent numerical results. The dimensionless time is defined as $t^* = t/\sqrt{L/g}$, and the Reynolds number $\mathrm{Re} = L\sqrt{Lg}/\nu$, in which g is the gravitational acceleration and ν is the kinematic viscosity of both fluids. The characteristic velocity of the system is set to $U = \sqrt{Lg} = 0.04$. Periodic boundary conditions are applied on the left and right boundaries, and the halfway bounce-back boundary conditions are used on the top and bottoms walls. The initial interface shape is given by $y = 2L + 0.1L\cos(2\pi x/L)$.

Figure 4 shows the time evolution of the interface shape for Re = 256, in which our simulation results are compared with those obtained by the original color-gradient model. At the initial stage ($t^* \leqslant 2$), the heavy fluid moves downward,

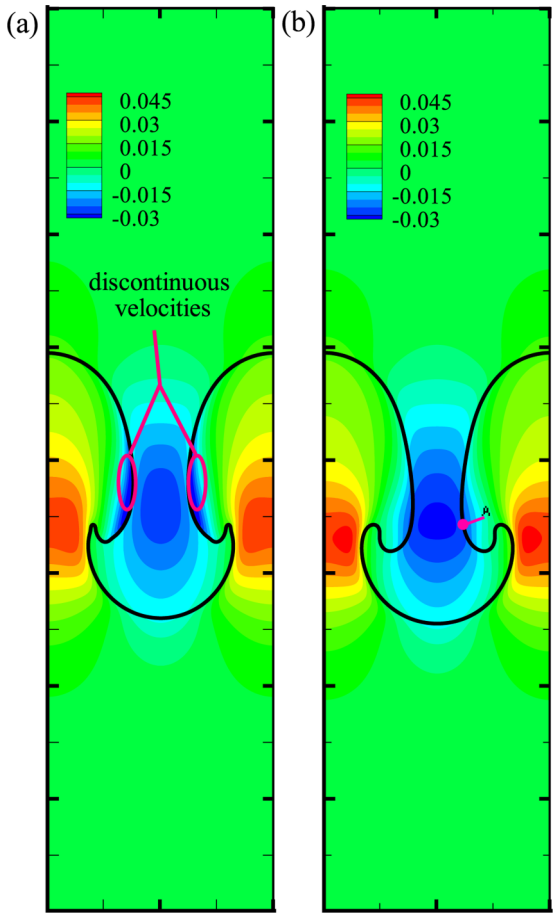

FIG. 5. Interface shapes ($\rho^N = 0$) and contours of the y component of the velocity at $t^* = 2.5$, which are obtained by (a) the original color-gradient model and (b) the present model.

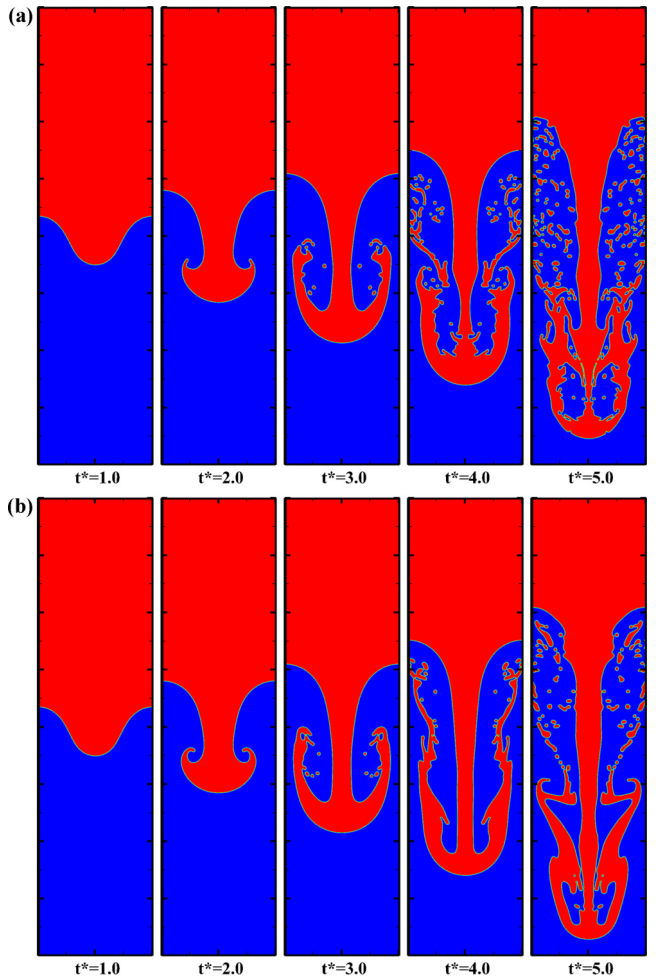

FIG. 6. Snapshots of the interface shape ($\rho^N = 0$) at different times for At = 0.5 and Re = 2048, obtained by (a) the original color-gradient model and (b) the present model.

forming a spike in the middle, and the light fluid forms bubbles on left and right sides. During this time, the simulation results of different models show the same interface shapes. As the spike rolls up and two side-spikes gradually grow ($t^* > 2$), the shapes of the bubble and spike fronts obtained by the original color-gradient model and our model become quite different, and the details of the interface obtained by our model are observed to be closer to the results of Figs. 8(a)–8(e) in Chiappini *et al.* [48]. Particularly, by looking at the contours of the y component of the velocity at $t^* = 2.5$ (which are plotted in Fig. 5), we find that there exist some obvious discontinuous velocities in the light fluid near the spike when the original color-gradient model is used. This may be caused by the error term in the original color-gradient model, which cannot be ignored since the downward velocity at the point **A** [see Fig. 5(b)] is as high as 0.027 under the effect of gravity.

Figure 6 shows the time evolution of the interface shape for Re = 2048 obtained by the original color-gradient model and the present model. Compared with the results in Fig. 4, the movements of the spike and bubble are similar and two side-spikes also appear in the initial stage. But at this Reynolds number, the interface suffers from the Kelvin-Helmholtz instability [41,44], and many secondary vortices appear near the two side-spikes. In addition, it is noticed in Fig. 6(a) that the original color-gradient model is not able to maintain a smooth interface in the late stage of the simulation due to the error term, i.e., Eq. (9). In contrast, smooth interfaces are obtained by our model [see Fig. 6(b)], and the interface shapes overall match with those of Figs. 8(f) and 8(g) in Chiappini *et al.* [48] at different times.

Figure 7 shows the positions of the spike bottom and the bubble top obtained by the original color-gradient model and our model, and the obtained results are compared with the data in previous studies [44,48]. For the position of the bubble top, the predicted results from both models agree well with the data in Refs. [44,48] since the velocity at this position

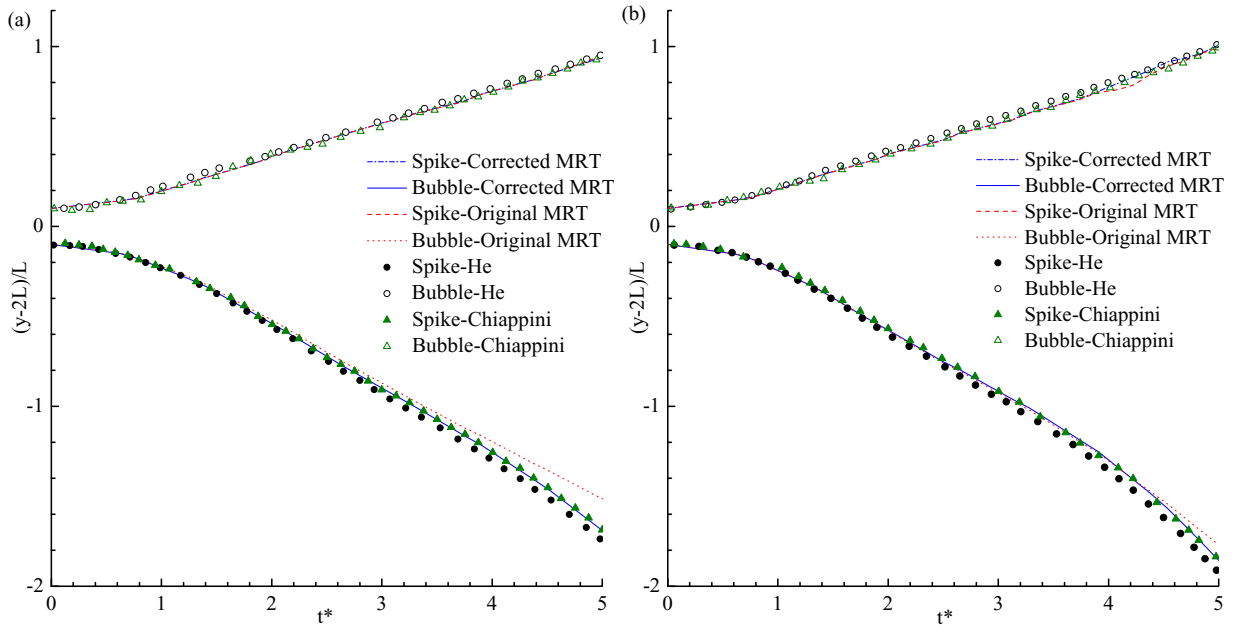

FIG. 7. Positions of the spike bottom and bubble top obtained by the present model and the original color-gradient model at At = 0.5 for (a) Re = 256 and (b) Re = 2048. The previous numerical results of He *et al.* [44] and Chiappini *et al.* [48] are also presented for comparison.

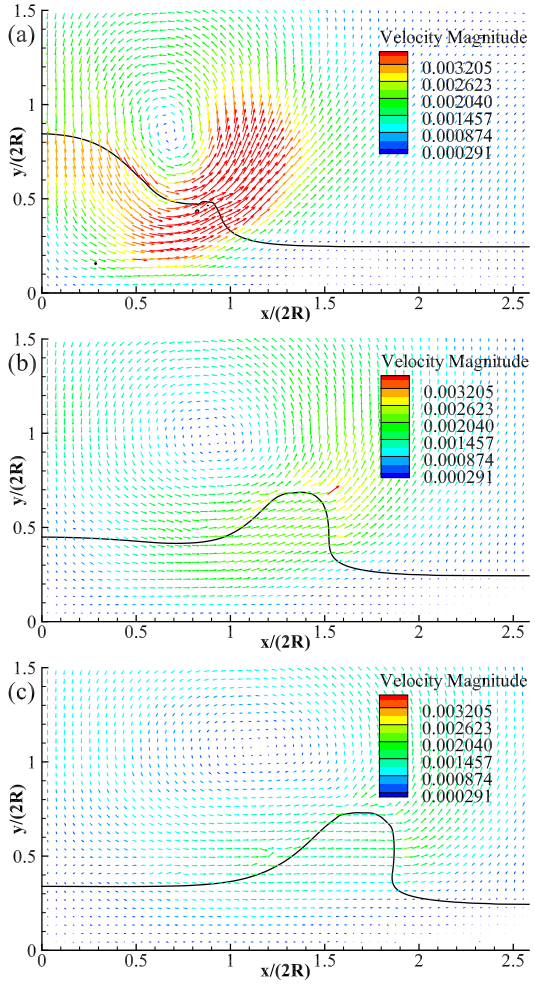

FIG. 8. Snapshots of the interface shape ($\rho^N = 0$) and the velocity field at (a) $t^* = 0.5$, (b) $t^* = 1.5$, and (c) $t^* = 2.5$ for Re = 40.

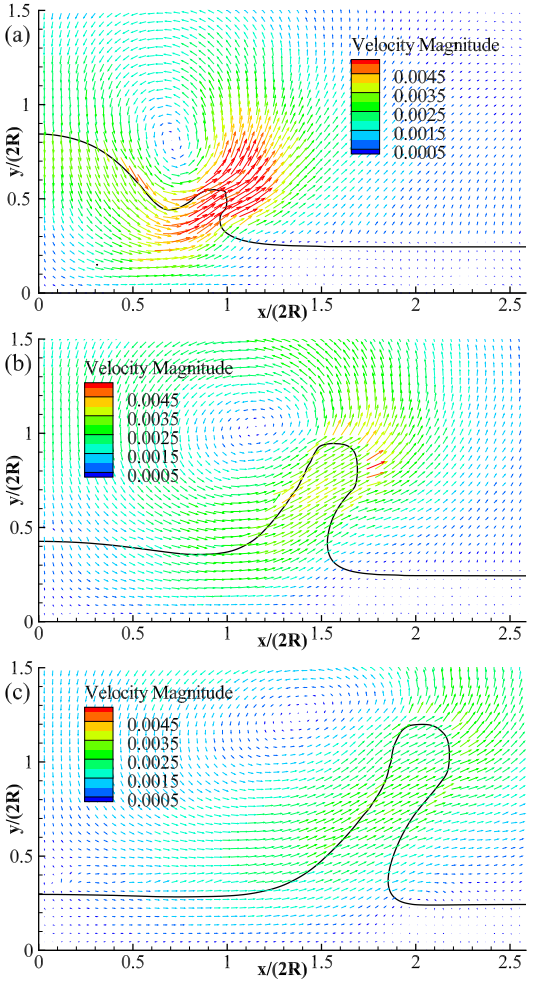

FIG. 9. Snapshots of the interface shape ($\rho^N = 0$) and the velocity field at (a) $t^* = 0.5$, (b) $t^* = 1.5$, and (c) $t^* = 2.5$ for Re = 100.

always keeps at a small value during the simulations. For the position of the spike bottom, the predicted results from the present model agree perfectly with those in Refs. [44,48], but the predicted results from the original color-gradient model gradually deviate from the available literature data with time, especially at Re = 256.

D. Droplet splashing on a thin liquid film

In this subsection, droplet splashing on a thin liquid film [49–53] with an initial velocity U is simulated. Droplet splashing is encountered in a variety of natural processes and engineering applications ranging from raindrop falling on the ground, ink-jet printing, to spray cooling in a combustion chamber. In the present simulations, the size of the computational domain is set as $2L \times L$, in which $L = 500$ lattice cells. A liquid layer of thickness $h = 0.1L$ is located over the bottom wall, and a circular droplet with the radius $R = 0.2L$ is initially located at $(L, 0.3L)$. The entire computational domain is initialized as the gas (blue fluid) except the droplet and the liquid film (red fluid). Periodic boundary conditions are applied at the left and right boundaries, and the halfway bounce-back boundary conditions are used at the top and bottom walls. The Reynolds number is defined as $\mathrm{Re} = UL/\nu^R$, Weber number is $\mathrm{We} = \rho^R U^2 L/\sigma$, and the dimensionless time is $t^* = tU/(2R)$. The parameter α^B is taken as 0.2, and β is set to 0.2 to keep the interface stable at high density ratios. This β corresponds to an interface thickness of 6–8 lattice grids, which is acceptable in the present simulation since the computational domain is sufficiently large. The initial droplet velocity is set to 0.005, and the Weber number in all cases is fixed at 160.

In this study the density ratio of 100 is considered, because if the density ratio is further increased, the simulation becomes unstable at high Reynolds numbers. Based on the previous studies of Mukherjee *et al.* [50] and Josserand *et al.* [51], the influence of the surrounding gas density on the evolution of the crown radius is insignificant for the density ratio larger than 50. This fact will allow us to quantitatively compare the simulation results with the previously developed scaling laws [49,51–53]. Reynolds numbers ranging from 40 to 500 are considered, and different Reynolds numbers are achieved by changing the dynamic viscosity of the droplet μ^R from 2.5 to 0.2 while keeping μ^B at 0.1. The simulation results obtained by the present model are shown only since the simulation becomes

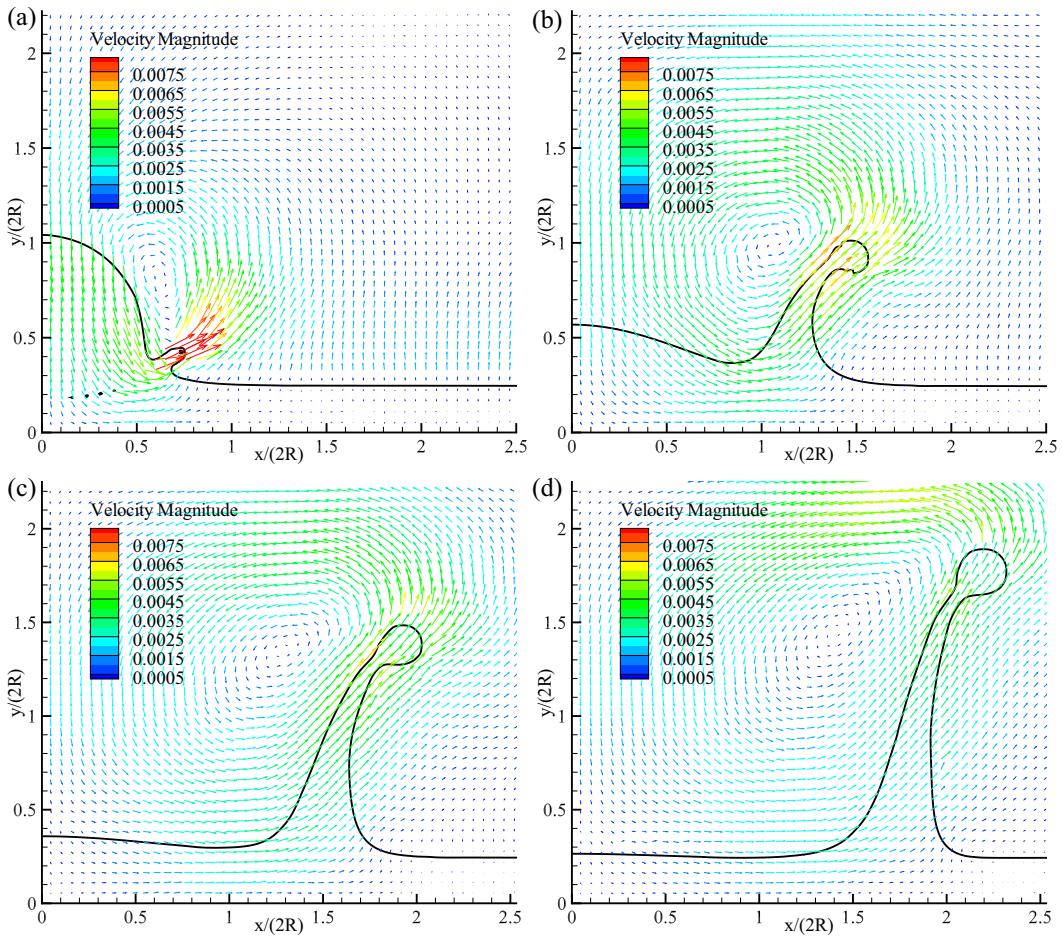

FIG. 10. Snapshots of the interface shape ($\rho^N = 0$) and the velocity field at (a) $t^* = 0.25$, (b) $t^* = 1$, (c) $t^* = 1.75$, and (d) $t^* = 2.5$ for Re = 500.

unstable after a few time steps for the original color-gradient model.

Figures 8–10 show the snapshots of the interface shape and the velocity filed at several typical times for Re = 40, Re = 100, and Re = 500, respectively. It can be observed that the droplet spreads on the liquid film gently without splashing for Re = 40, whereas for larger Re a thin liquid sheet is emitted after the droplet impacts and then grows into a crown. For all Reynolds numbers considered, the velocity magnitude decreases with time due to the viscous force from the gas phase, and a vortex is observed between the liquid sheet and the central droplet, which is formed due to the falling down of the droplet and the rising up of the liquid sheet. This vortex causes the sheet to move inward and eventually to become nearly normal to the substrate in the duration of the simulation. In addition, with increasing Re, the liquid sheet gets thinner and becomes more perpendicular to the substrate because the overall velocity magnitude inside the vortex grows with Re.

In the droplet splashing process, the spreading factor $r/(2R)$ was found to exhibit a power law dependence on the dimensionless time t^*, i.e., $r/(2R) = C\sqrt{t^*}$, in which r is the spreading radius, and C is a constant. Also, a number of studies have shown that C is usually in the range of 1.1–1.3 [49,51–53]. In Fig. 11 we plot the crown radius as

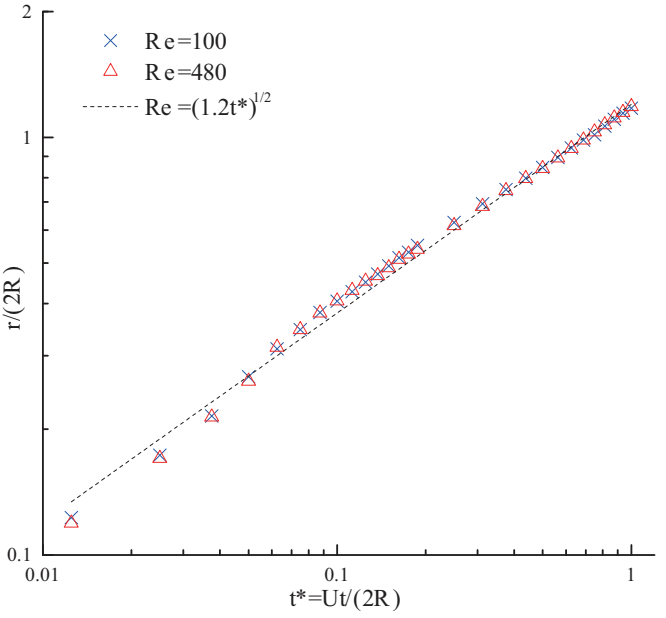

FIG. 11. Dimensionless spreading radius as a function of the dimensionless time at Re = 100 and 500. The spreading radius is normalized by $2R$.

a function of t^* for both Re = 100 and 500. It is seen that our data can be well fitted by a power law with the spreading factor $C = 1.2$, which is consistent with the previous findings.

Finally, it should be noted that the present MRT collision operator is compatible with its BGK counterpart. However, according to our tests, the BGK operator has poorer numerical stability in general. With the BGK collision operator, for example, stable numerical results can be achieved for the static droplet and layered channel flows up to the density ratio of 100, the Rayleigh Taylor instability test for the density ratio of 3 up to the Reynolds number of 800, and the droplet splashing test for the density of 10 up to Re = 400.

IV. CONCLUSIONS

The simulation of two-component flows with high density ratio and high Reynolds number still remains a challenge for many multiphase LB models. In this paper we develop a color-gradient LB model for simulating two-phase flows with high density ratio. The model applies a MRT collision operator to enhance the stability of the simulation. In order to recover the correct NSEs, we propose to add a simple source term into the single phase collision operator and use an equilibrium density distribution function that is derived from the third-order Hermite expansion of the Maxwellian distribution [30,34]. In addition, we introduce a phase field function to identify different fluids and use a MRT version of perturbation operator to realize the interfacial tension effect. We also follow the previous work of Latva Kokko and Rothman [19] and adopt their recoloring operator to ensure the immiscibility of both fluids.

To validate the model, we first simulate the steady flows with theoretical solutions, i.e., a static droplet and the layered channel flow. In the static droplet test, we find that the predicted interfacial tension agrees well with the analytical solution, and the maximum value of spurious velocities is on the order of 10^{-5} for $\gamma < 100$ and on the order of 10^{-4} for $\gamma = 1000$. In the layered channel flow, we use the original color-gradient model and the present model to predict the velocity profiles, and find that the present model can provide satisfactory predictions of the velocity profiles for the density ratios up to 1000 but the original color-gradient model produces large deviation from the analytical solution due to unwanted error term in the recovered NSEs. Then, two cases of unsteady flows, namely Rayleigh-Taylor instability and a droplet splashing on a thin film, are simulated. In the former test, the density ratio of 3 with the Reynolds numbers of 256 and 2048 are considered. In comparison with the original color-gradient model, the interface shapes obtained by the present model match better with those obtained by Chiappini *et al.* [48]. Also, the interface positions of the spike and bubble predicted by the present model are in quantitative agreement with the previous numerical results [44,48]. In the latter test, the density of 100 and Reynolds numbers up to 500 are considered. Consistent with the previous studies [51,53], the spreading radius is found to exhibit a power law dependence on the time for different Reynolds numbers.

ACKNOWLEDGMENTS

The authors acknowledge the support from National Natural Science Foundation of China under Grants No. 51576148 and No. 51506168, and from LANL's LDRD Program and Institutional Computing Program. Y.B. would like to acknowledge the financial support from the China Scholarship Council. H.L. gratefully acknowledges the support from the "Young Thousand Talents Program" of China.

APPENDIX A: THE TRANSFORMATION MATRIX AND ITS INVERSE MATRIX

$$\mathbf{M} = \begin{bmatrix} 1 & 1 & 1 & 1 & 1 & 1 & 1 & 1 & 1 \\ -4 & -1 & -1 & -1 & -1 & 2 & 2 & 2 & 2 \\ 4 & -2 & -2 & -2 & -2 & 1 & 1 & 1 & 1 \\ 0 & 1 & 0 & -1 & 0 & 1 & -1 & -1 & 1 \\ 0 & -2 & 0 & 2 & 0 & 1 & -1 & -1 & 1 \\ 0 & 0 & 1 & 0 & -1 & 1 & 1 & -1 & -1 \\ 0 & 0 & -2 & 0 & 2 & 1 & 1 & -1 & -1 \\ 0 & 1 & -1 & 1 & -1 & 0 & 0 & 0 & 0 \\ 0 & 0 & 0 & 0 & 0 & 1 & -1 & 1 & -1 \end{bmatrix}, \tag{A1}$$

$$\mathbf{M}^{-1} = \frac{1}{36}\begin{bmatrix} 4 & -4 & 4 & 0 & 0 & 0 & 0 & 0 & 0 \\ 4 & -1 & -2 & 6 & -6 & 0 & 0 & 9 & 0 \\ 4 & -1 & -2 & 0 & 0 & 6 & -6 & -9 & 0 \\ 4 & -1 & -2 & -6 & 6 & 0 & 0 & 9 & 0 \\ 4 & -1 & -2 & 0 & 0 & -6 & 6 & -9 & 0 \\ 4 & 2 & 1 & 6 & 3 & 6 & 3 & 0 & 9 \\ 4 & 2 & 1 & -6 & -3 & 6 & 3 & 0 & -9 \\ 4 & 2 & 1 & -6 & -3 & -6 & -3 & 0 & 9 \\ 4 & 2 & 1 & 6 & 3 & -6 & -3 & 0 & -9 \end{bmatrix}. \tag{A2}$$

APPENDIX B: DEVIATION OF THE SINGLE PHASE COLLISION OPERATOR USING THE CHAPMAN-ENSKOG EXPANSION

In this Appendix we present the Chapman-Enskog analysis to demonstrate that the source term $\mathbf{C}^k$ proposed in Eq. (17) can correctly recover the NSEs [54].

In absence of the perturbation and segregation operators, the collision operator $\mathbf{\Omega}_i^k$ in can be simplified as $(\mathbf{\Omega}_i^k)^{(1)}$ expressed by Eq. (11). Thus, the evolution equation without the perturbation and segregation operators can be written as

$$f_i^k(\mathbf{x}+\mathbf{e}_i\delta_t,t+\delta_t) = f_i^k(\mathbf{x},t) - \sum_j (\mathbf{M}^{-1}\mathbf{S}^k)_{ij}\left[m_j^k(\mathbf{x},t) - m_j^{k,(\mathrm{eq})}(\mathbf{x},t)\right] + \sum_j (\mathbf{M}^{-1})_{ij} C_j^k(\mathbf{x},t). \tag{B1}$$

Taking the sum of Eq. (B1) over k, we get

$$f_i(\mathbf{x}+\mathbf{e}_i\delta_t,t+\delta_t) = f_i(\mathbf{x},t) - \sum_j (\mathbf{M}^{-1}\mathbf{S})_{ij}\left[m_j(\mathbf{x},t) - m_j^{(\mathrm{eq})}(\mathbf{x},t)\right] + \sum_j (\mathbf{M}^{-1})_{ij} C_j(\mathbf{x},t), \tag{B2}$$

in which $m_j^{(\mathrm{eq})}(\mathbf{x},t) = \sum_k m_j^{k,(\mathrm{eq})}(\mathbf{x},t)$, and $C_j(\mathbf{x},t) = \sum_k C_j^k(\mathbf{x},t)$. In the moment space, Eq. (B2) can be expressed as

$$\mathbf{m}(\mathbf{x}+\mathbf{e}_i\delta_t,t+\delta_t) = \mathbf{m}(\mathbf{x},t) - \mathbf{S}[\mathbf{m}(\mathbf{x},t) - \mathbf{m}^{(\mathrm{eq})}(\mathbf{x},t)] + \mathbf{C}(\mathbf{x},t), \tag{B3}$$

where the equilibrium moment functions are listed in Eq. (16). Then we expand the moment function, the derivatives of time and space, and the source term in consecutive scales of ε,

$$\mathbf{m} = \mathbf{m}^{(0)} + \varepsilon\mathbf{m}^{(1)} + \varepsilon^2\mathbf{m}^{(2)} + \cdots, \quad \partial_t = \varepsilon\partial_{t0} + \varepsilon^2\partial_{t1}, \quad \partial_\alpha = \varepsilon\partial_{0\alpha}, \quad \mathbf{C} = \varepsilon\mathbf{C}^{(0)}, \tag{B4}$$

where ε is a small parameter. Applying Taylor expansion to Eq. (B4) and using Eq. (B5), one can obtain the zero-, first-, and second-order equations in ε,

$$\varepsilon^0 : \ \mathbf{m}^{(0)} = \mathbf{m}^{(\mathrm{eq})}, \tag{B5a}$$

$$\varepsilon^1 : \ \widehat{\mathbf{D}}_0\mathbf{m}^{(0)} = -\mathbf{S}'\mathbf{m}^{(1)} + \mathbf{C}^{(0)}, \tag{B5b}$$

$$\varepsilon^2 : \ \partial_{t1}\mathbf{m}^{(0)} + \widehat{\mathbf{D}}_0\mathbf{m}^{(1)} + \frac{\delta_t}{2}\widehat{\mathbf{D}}_0^2\mathbf{m}^{(0)} = -\mathbf{S}'\mathbf{m}^{(2)}, \tag{B5c}$$

where $\mathbf{S}' = \mathbf{S}/\delta_t$, $\widehat{\mathbf{D}}_0 = \mathbf{M}\mathbf{D}_0\mathbf{M}^{-1}$, and $\mathbf{D}_0 = \partial_{t0} + \partial_{\alpha 0}\mathrm{diag}(e_{0\alpha}, e_{1\alpha}, \ldots, e_{8\alpha})$. Combining Eq. (B5b) with Eq. (B5c), one easily obtains

$$\varepsilon^2 : \ \partial_{t1}\mathbf{m}^{(0)} + \widehat{\mathbf{D}}_0\left(\mathbf{I} - \frac{\mathbf{S}}{2}\right)\mathbf{m}^{(1)} + \frac{\delta_t}{2}\widehat{\mathbf{D}}_0\mathbf{C}^{(0)} = -\mathbf{S}'\mathbf{m}^{(2)}. \tag{B5d}$$

Since the conservative moments m_0, m_4, and m_6 satisfy the following equations:

$$\rho^{(n)} = j_x^{(n)} = j_y^{(n)} = 0, \ \ n > 0, \tag{B6}$$

Eq. (B5b) can be written explicitly as

$$\partial_{t_0}\begin{bmatrix} \rho \\ \sum_k \rho^k(-3.6\alpha^k - 0.4 + 3u^2) \\ \sum_k \rho^k(5.4\alpha^k - 1.4 - 3u^2) \\ \rho u_x \\ \sum_k (-0.2 - 1.8\alpha^k)\rho^k u_x \\ \rho u_y \\ \sum_k (-0.2 - 1.8\alpha^k)\rho^k u_y \\ \rho\left(u_x^2 - u_y^2\right) \\ \rho u_x u_y \end{bmatrix} + \partial_{0x}\begin{bmatrix} \rho u_x \\ \sum_k (0.8 - 1.8\alpha^k)\rho^k u_x \\ \sum_k (-0.2 - 1.8\alpha^k)\rho^k u_x \\ p + \rho u_x^2 \\ -p - \rho\left(u_x^2 - u_y^2\right) \\ \rho u_x u_y \\ \rho u_x u_y \\ \sum_k (0.4 + 0.6\alpha^k)\rho^k u_x \\ p u_y \end{bmatrix} + \partial_{0y}\begin{bmatrix} \rho u_y \\ \sum_k (0.8 - 1.8\alpha^k)\rho^k u_y \\ \sum_k (-0.2 - 1.8\alpha^k)\rho^k u_y \\ \rho u_x u_y \\ \rho u_x u_y \\ p + \rho u_y^2 \\ -p + \rho\left(u_x^2 - u_y^2\right) \\ -\sum_k (0.4 + 0.6\alpha^k)\rho^k u_y \\ p u_x \end{bmatrix} = \begin{bmatrix} 0 \\ -s_e' e^{(1)} \\ -s_\varepsilon' \varepsilon^{(1)} \\ 0 \\ -s_q' q_x^{(1)} \\ 0 \\ -s_q' q_y^{(1)} \\ -s_\nu' p_{xx}^{(1)} \\ -s_\nu' p_{xy}^{(1)} \end{bmatrix} + \begin{bmatrix} C_0^{(0)} \\ C_1^{(0)} \\ C_2^{(0)} \\ C_3^{(0)} \\ C_4^{(0)} \\ C_5^{(0)} \\ C_6^{(0)} \\ C_7^{(0)} \\ C_8^{(0)} \end{bmatrix}, \tag{B7}$$

and Eq. (B5d) as

$$\partial_{t1}\rho + C_0^{(0)} = 0, \tag{B8a}$$

$$\partial_{t1}(\rho u_x) + \frac{1}{6}\left(1 - \frac{s_e}{2}\right)\partial_{0x}[e^{(1)}] + \left(1 - \frac{s_\nu}{2}\right)\left[\frac{1}{2}\partial_{0x}p_{xx}^{(1)} + \partial_{0y}p_{xy}^{(1)}\right] + \frac{\delta_t}{2}\left(\partial_{t0}C_3^{(0)} + \frac{2}{3}\partial_{0x}C_0^{(0)} + \frac{1}{6}\partial_{0x}C_1^{(0)} + \frac{1}{2}\partial_{0x}C_7^{(0)} + \partial_{0y}C_8^{(0)}\right) = 0, \tag{B8b}$$

$$\partial_{t1}(\rho u_y) + \frac{1}{6}\left(1 - \frac{s_e}{2}\right)\partial_{0y}[e^{(1)}] + \left(1 - \frac{s_v}{2}\right)\left[-\frac{1}{2}\partial_{0y}p_{xx}^{(1)} + \partial_{0x}p_{xy}^{(1)}\right] + \frac{\delta_t}{2}\left(\partial_{t0}C_3^{(0)} + \frac{2}{3}\partial_{0y}C_0^{(0)} + \frac{1}{6}\partial_{0y}C_1^{(0)} - \frac{1}{2}\partial_{0y}C_7^{(0)} + \partial_{0x}C_8^{(0)}\right) = 0, \tag{B8c}$$

in which the source term $\mathbf{C}^{(0)} = \sum_k \mathbf{C}^{(0),k} = \sum_k \mathbf{C}^k$ is calculated by Eq. (17). In what follows we will prove that this source term can recover the exact NSEs.

The macroscopic governing equations at t_0 scale can be directly obtained from the first, fourth, and sixth equations in Eq. (B7) with $C_0^{(0)} = C_3^{(0)} = C_5^{(0)} = 0$ as

$$\partial_{t0}\rho + \partial_{0x}(\rho u_x) + \partial_{0y}(\rho u_y) = 0, \tag{B9a}$$

$$\partial_{t0}(\rho u_x) + \partial_{0x}(\rho u_x u_x) + \partial_{0y}(\rho u_x u_y) = -\partial_{0x}p, \tag{B9b}$$

$$\partial_{t0}(\rho u_y) + \partial_{0x}(\rho u_x u_y) + \partial_{0y}(\rho u_y u_y) = -\partial_{0y}p. \tag{B9c}$$

Substituting Eq. (17) into the second, eighth, and ninth equations of Eq. (B7) leads to the following equations:

$$-s_e' e^{(1)} = 6p(\partial_{0x}u_x + \partial_{0y}u_y) + \frac{3s_e}{2}\sum_k (0.8 - 1.8\alpha^k)[\partial_{0x}(\rho^k u_x) + \partial_{0y}(\rho^k u_y)], \tag{B10a}$$

$$-s_v' p_{xx}^{(1)} = 2p(\partial_{0x}u_x - \partial_{0y}u_y) + \frac{s_v}{2}\sum_k (0.8 - 1.8\alpha^k)[\partial_{0x}(\rho^k u_x) + \partial_{0y}(\rho^k u_y)], \tag{B10b}$$

$$-s_v' p_{xy}^{(1)} = p(\partial_{0x}u_y + \partial_{0y}u_x). \tag{B10c}$$

Then, substituting Eqs. (B10a)–(B10c) and (17) into Eqs. (B8a)–(B8c), one can obtain

$$\partial_{t1}\rho = 0, \tag{B11a}$$

$$\partial_{t1}(\rho u_x) + \delta_t\left(\frac{1}{s_e} - \frac{1}{2}\right)\partial_{0x}[p(\partial_{0x}u_x + \partial_{0y}u_y)] + \delta_t\left(\frac{1}{s_v} - \frac{1}{2}\right)\partial_{0x}[p(\partial_{0x}u_x - \partial_{0y}u_y)] + \delta_t\left(\frac{1}{s_v} - \frac{1}{2}\right)\partial_{0y}[p(\partial_{0x}u_y + \partial_{0y}u_x)] = 0, \tag{B11b}$$

$$\partial_{t1}(\rho u_y) + \delta_t\left(\frac{1}{s_e} - \frac{1}{2}\right)\partial_{0y}[p(\partial_{0x}u_x + \partial_{0y}u_y)] + \delta_t\left(\frac{1}{s_v} - \frac{1}{2}\right)\partial_{0y}[p(\partial_{0x}u_x - \partial_{0y}u_y)] + \delta_t\left(\frac{1}{s_v} - \frac{1}{2}\right)\partial_{0x}[p(\partial_{0x}u_y + \partial_{0y}u_x)] = 0. \tag{B11c}$$

In this way we can obtain the following momentum equations at t_1 scale:

$$\partial_{t1}(\rho u_x) = \partial_{0x}\tau_{xx}^{(0)} + \partial_{0y}\tau_{xy}^{(0)}, \tag{B12a}$$

$$\partial_{t1}(\rho u_y) = \partial_{0x}\tau_{xy}^{(0)} + \partial_{0y}\tau_{yy}^{(0)}, \tag{B12b}$$

where

$$\tau_{xx}^{(0)} = \delta_t\left(\frac{1}{s_e} - \frac{1}{2}\right)(\partial_{0x}u_x + \partial_{0y}u_y)p + \delta_t\left(\frac{1}{s_v} - \frac{1}{2}\right)(\partial_{0x}u_x - \partial_{0y}u_y)p, \tag{B13a}$$

$$\tau_{xy}^{(0)} = \delta_t\left(\frac{1}{s_v} - \frac{1}{2}\right)(\partial_{0x}u_y + \partial_{0y}u_x)p, \tag{B13b}$$

$$\tau_{yy}^{(0)} = \delta_t\left(\frac{1}{s_e} - \frac{1}{2}\right)(\partial_{0x}u_x + \partial_{0y}u_y)p - \delta_t\left(\frac{1}{s_v} - \frac{1}{2}\right)(\partial_{0x}u_x - \partial_{0y}u_y)p. \tag{B13c}$$

Combining the equations at t_0 and t_1 scales, the following macroscopic equations can be recovered, i.e.,

$$\partial_t(\rho) + \nabla\cdot(\rho\mathbf{u}) = 0, \tag{B14a}$$

$$\partial_t(\rho\mathbf{u}) + \nabla\cdot(\rho\mathbf{u}\mathbf{u}) = -\nabla p + \nabla\cdot\boldsymbol{\tau}, \tag{B14b}$$

where $\boldsymbol{\tau} = 2\mu\mathbf{S} + (\xi - \mu)(\nabla\cdot\mathbf{u})\mathbf{I}$, $\varsigma = \delta_t(\frac{1}{s_e} - \frac{1}{2})p$ is the bulk viscosity, $\mu = \delta_t(\frac{1}{s_v} - \frac{1}{2})p$ is the dynamic viscosity, and $\mathbf{S} = \frac{1}{2}[\nabla\mathbf{u} + (\nabla\mathbf{u})^T]$ is the strain rate tensor.

From Eqs. (B14a) and (B14b), it is clearly seen that the target NSEs is exactly recovered with the proposed source term $\mathbf{C}^k$ given in Eq. (17).

[1] S. Chen and G. D. Doolen, Annu. Rev. Fluid Mech. **30**, 329 (1998).
[2] C. K. Aidun and J. R. Clausen, in *Annual Review of Fluid Mechanics* (Annual Reviews, Palo Alto, 2010), pp. 439.
[3] Q. Li, K. Luo, Q. Kang, Y. He, Q. Chen, and Q. Liu, Progress Energy Combust. Sci. **52**, 62 (2015).
[4] C. W. Hirt and B. D. Nichols, J. Comput. Phys. **39**, 201 (1981).
[5] T. W. H. Sheu, C. H. Yu, and P. H. Chiu, J. Comput. Phys. **228**, 661 (2009).
[6] M. Sussman, P. Smereka, and S. Osher, J. Comput. Phys. **114**, 146 (1994).
[7] S. Osher and R. P. Fedkiw, J. Comput. Phys. **169**, 463 (2001).
[8] A. K. Gunstensen, D. H. Rothman, S. Zaleski, and G. Zanetti, Phys. Rev. A **43**, 4320 (1991).
[9] X. Shan and H. Chen, Phys. Rev. E **47**, 1815 (1993).
[10] L. Chen, Q. Kang, Y. Mu, Y. He, and W. Tao, Int. J. Heat Mass Transfer **76**, 210 (2014).
[11] Q. Kang, D. Zhang, and S. Chen, Phys. Fluids **14**, 3203 (2002).
[12] M. R. Swift, E. Orlandini, W. R. Osborn, and J. M. Yeomans, Phys. Rev. E **54**, 5041 (1996).
[13] X. He, X. Shan, and G. D. Doolen, Phys. Rev. E **57**, R13 (1998).
[14] R. Zheng, H. Liu, J. Sun, and Y. Ba, Physica A **411**, 53 (2014).
[15] T. Reis and T. N. Phillips, J. Phys. A **40**, 4033 (2007).
[16] H. Liu, A. J. Valocchi, and Q. Kang, Phys. Rev. E **85**, 046309 (2012).
[17] D. H. Rothman and J. M. Keller, J. Stat. Phys. **52**, 1119 (1988).
[18] D. Grunau, S. Y. Chen, and K. Eggert, Phys. Fluids A **5**, 2557 (1993).
[19] M. Latva-Kokko and D. H. Rothman, Phys. Rev. E **71**, 056702 (2005).
[20] S. V. Lishchuk, C. M. Care, and I. Halliday, Phys. Rev. E **67**, 036701 (2003).
[21] H. Liu, A. J. Valocchi, C. Werth, Q. Kang, and M. Oostrom, Adv. Water Res. **73**, 144 (2014).
[22] H. Liu and Y. Zhang, Phys. Fluids **23**, 082101 (2011).
[23] A. Gupta and R. Kumar, Microfluidics Nanofluidics **8**, 799 (2010).
[24] S. Leclaire, M. Reggio, and J. Y. Trepanier, Appl. Math. Model. **36**, 2237 (2012).
[25] H. Huang, J. Huang, X. Lu, and M. Sukop, Int. J. Mod. Phys. C **24**, 1350021 (2013).
[26] S. Leclaire, N. Pellerin, M. Reggio, and J. Y. Trepanier, Int. J. Multiphase Flow **57**, 159 (2013).
[27] S. V. Lishchuk, I. Halliday, and C. M. Care, Phys. Rev. E **77**, 036702 (2008).
[28] P. Lallemand and L. S. Luo, Phys. Rev. E **61**, 6546 (2000).
[29] H. Huang, J. Huang, and X. Lu, Comput. Fluids **93**, 164 (2014).
[30] X. W. Shan, X. F. Yuan, and H. D. Chen, J. Fluid Mech. **550**, 413 (2006).
[31] S. Leclaire, N. Pellerin, M. Reggio, and J. Y. Trepanier, J. Phys. A **47**, 105501 (2014).
[32] T. Inamuro, T. Ogata, S. Tajima, and N. Konishi, J. Comput. Phys. **198**, 628 (2004).
[33] T. Lee and C. L. Lin, J. Comput. Phys. **206**, 16 (2005).
[34] Q. Li, K. H. Luo, Y. L. He, Y. J. Gao, and W. Q. Tao, Phys. Rev. E **85**, 016710 (2012).
[35] Y. Ba, H. Liu, J. Sun, and R. Zheng, Phys. Rev. E **88**, 043306 (2013).
[36] S. Leclaire, M. Reggio, and J. Y. Trepanier, J. Comput. Phys. **246**, 318 (2013).
[37] Z. Guo, C. Zheng, and B. Shi, Phys. Rev. E **65**, 046308 (2002).
[38] I. Halliday, A. P. Hollis, and C. M. Care, Phys. Rev. E **76**, 026708 (2007).
[39] A. P. Hollis, I. Halliday, and R. Law, Phys. Rev. E **76**, 026709 (2007).
[40] J. Tolke, X. Krafczyk, M. Schulz, and E. Rank, Philos. Trans. R. Soc. London Ser. A **360**, 535 (2002).
[41] T. Lee and L. Liu, J. Comput. Phys. **229**, 8045 (2010).
[42] A. J. Ladd, J. Fluid Mech. **271**, 285 (1994).
[43] Q. Kang, D. Zhang, and S. Chen, Adv. Water Res. **27**, 13 (2004).
[44] X. He, S. Chen, and R. Zhang, J. Comput. Phys. **152**, 642 (1999).
[45] H. Ding, P. D. M. Spelt, and C. Shu, J. Comput. Phys. **226**, 2078 (2007).
[46] S. Leclaire, M. Reggio, and J. Y. Trepanier, Comput. Fluids **48**, 98 (2011).
[47] Q. Li, K. H. Luo, Y. J. Gao, and Y. L. He, Phys. Rev. E **85**, 026704 (2012).
[48] D. Chiappini, G. Bella, S. Succi, F. Toschi, and S. Ubertini, Commun. Comput. Phys. **7**, 423 (2010).
[49] A. L. Yarin, in *Annual Review of Fluid Mechanics* (Annual Reviews, Palo Alto, 2006), pp. 159.
[50] S. Mukherjee and J. Abraham, Phys. Fluids **19**, 052103 (2007).
[51] C. Josserand and S. Zaleski, Phys. Fluids **15**, 1650 (2003).
[52] J. Shao and C. Shu, Int. J. Numer. Methods Fluids **77**, 526 (2015).
[53] Q. Li, K. H. Luo, and X. J. Li, Phys. Rev. E **87**, 053301 (2013).
[54] Z. Chai and T. S. Zhao, Phys. Rev. E **86**, 016705 (2012).